

# Organic Semiconductor Single Crystals for X-ray Imaging

Mingxi Chen, Lingjie Sun, Xiangyu Ou, Huanghao Yang, Xiaogang Liu, Huanli Dong, Wenping Hu,\* and Xiangfeng Duan\*

Low-dose, high-resolution X-ray imaging is vital for medical diagnostics and material/device analyses. Current X-ray imagers are dominated by expensive inorganic materials via high-temperature solid processes (up to 1700 °C, e.g., CsI:Tl) with heavy metal elements. It is essential to search for new materials as X-ray imagers with low growth temperature, low cost, high sensitivity, along with high chemical and environmental stability. Here, 9,10-diphenylanthracene (9,10-DPA) single crystals are used as a representative model, which are grown via low-temperature solution processes, exhibiting intense X-ray radioluminescence with ultrahigh photon-conversion efficiency, ultrafast response and high sensitivity. The resolution of devices based on organic crystals exceeds 20.00 lp mm<sup>-1</sup>. Meanwhile the crystals exhibit high cycle performance under X-ray irradiation and environmental stability. This study demonstrates that organic semiconductors have potential use in low-cost, high-sensitivity and low-dose X-ray imaging systems.

## 1. Introduction

X-ray detectors have been widely studied and used in industrial and medical applications, including radiography, computed tomography, and scientific research,<sup>[1–4]</sup> since X-rays were discovered by Wilhelm Röntgen in the 1890s.<sup>[5,6]</sup> Generally, X-ray detectors can be classified into direct and indirect types, and the latter is cheaper and more stable than the former.<sup>[7,8]</sup> Scintillators can convert radiation (e.g., high-energy X-rays) into low-energy visible light, playing a decisive role in indirect X-ray imaging, computed tomography, and other fields.<sup>[9]</sup> A series of inorganic scintillators such as NaI:Tl, CsI:Tl, and bismuth germanate (Bi<sub>4</sub>Ge<sub>3</sub>O<sub>12</sub>) have been successfully applied in X-ray imaging,<sup>[10–13]</sup>

but they are generally grown at ultrahigh temperatures of ≈1700 °C using the Czochralski method.<sup>[14–16]</sup> Moreover, a delicate packaging process is required because of the hygroscopic nature and rapid degradation of these materials under ambient conditions.<sup>[17,18]</sup> Hence, it is essential to search for new scintillators with low growth temperature, low cost, high sensitivity, along with high chemical and environmental stability.<sup>[19–21]</sup>

Organic semiconductors have garnered significant attention as the cornerstone of organic electronics,<sup>[22]</sup> but no significant emphasis has been put on radiation detection because they consist of light elements with low absorption coefficients, and they are always believed to be unsuitable for this target.<sup>[11]</sup> In the present study, we demonstrate that this stereotype can be broken through single crystals of organic semiconductors. 9,10-diphenylanthracene (9,10-DPA) single crystals are used as a representative model, which are grown via low-temperature solution processes, exhibiting intense X-ray radioluminescence with ultrahigh photon-conversion efficiency (>5.3 times higher than that of the same thickness of CsI:Tl), ultrafast response (decay time of 1.63 ns vs ≈1000 ns of CsI:Tl), no significant afterglow interference, and short dead time, making it ideally suitable for highly sensitive (with 380 times lower dose rate than that in today's commercial X-ray diagnostics), high-resolution (resolution > 20.00 lp mm<sup>-1</sup>) instantaneous X-ray imaging. Additionally, the low absorption and high photon-conversion efficiency reduce the radiation damage to ensure excellent cycle performance. This study demonstrates that organic semiconductors can be used for low-cost, high-sensitivity, and low-dose X-ray imaging.

M. Chen, L. Sun, W. Hu  
Tianjin Key Laboratory of Molecular Optoelectronic Sciences  
Department of Chemistry  
School of Sciences  
Tianjin University  
Tianjin 300072, China  
E-mail: huwp@tju.edu.cn


X. Ou, H. Yang  
MOE Key Laboratory for Analytical Science of Food Safety and Biology  
Fujian Provincial Key Laboratory of Analysis and Detection Technology  
for Food Safety  
Fuzhou 350207, China

X. Liu  
Department of Chemistry  
National University of Singapore  
Singapore 117543, Singapore

X. Liu, W. Hu  
Joint School of National University of Singapore and Tianjin University  
International Campus of Tianjin University  
Binhai New City  
Fuzhou 350207, China

H. Dong  
Beijing National Research Center for Molecular Sciences  
Key Laboratory of Organic Solids  
Institute of Chemistry  
Chinese Academy of Sciences  
Beijing 100190, China

X. Duan  
Department of Chemistry & Biochemistry  
University of California at Los Angeles  
Los Angeles, CA 90095, USA  
E-mail: xduan@chem.ucla.edu

 The ORCID identification number(s) for the author(s) of this article can be found under <https://doi.org/10.1002/adma.202104749>.

DOI: 10.1002/adma.202104749

**Table 1.** Scintillation characteristics of different materials.

Materials	Emission max. [nm]	FWHM [nm]	Thickness [mm]	Decay time [ns]	$T_{\text{growth}}$ [°C]	Ref.
9,10-DPA	463	≈40	≈1	1.63	≈65	This work
CsI:TI	535	≈190	≈1	≈10 <sup>3</sup>	≈1700	[23]
PbWO <sub>4</sub>	440	≈110	≈1	≈10	≈1700	[24]
Bi <sub>4</sub> Ge <sub>3</sub> O <sub>12</sub>	498	≈140	≈1	≈10 <sup>2</sup>	≈1000	[25]
CaF <sub>2</sub> :Eu	440	≈40	≈1	10 <sup>2</sup> –10 <sup>4</sup>	≈1700	[26]
YAlO <sub>3</sub> :Ce	383	≈65	≈1	10 <sup>2</sup> –10 <sup>4</sup>	≈1700	[27]

## 2. Results and Discussions

A space-confined crystallizer was used to grow 9,10-DPA crystals by a gradient cooling process at 65 °C via a solution process (see the “Experimental Section” and also Figure S1 in the Supporting Information). The mild temperature is friendly, cost-effective, and conducive to control, which is of considerable advantage over today’s conventional inorganic scintillators that are normally grown at ultrahigh temperatures of ≈1700 °C using the Czochralski method (Table 1).<sup>[14–16,23–27]</sup> The obtained organic crystals with sizes up to several centimeters (Figure 1a–c) were identified as monoclinic crystals belonging to *C2/c* (Table S1, Supporting Information) with a unique

molecular packing structure (Figure 1d,e). The molecules have large torsion angles (up to 66.26°) between the phenyl groups and anthracene core, and massive intermolecular C–H··· $\pi$  interactions between adjacent molecules, which restrict the free rotation of the phenyl rings, block nonradiative channels, and prevent the quenching of its fluorescence to ensure strong radioluminescence.<sup>[28–31]</sup> The resulting crystals exhibited a yellowish color under room light (Figure 1a,c) and bright blue radioluminescence under X-ray beam excitation (Figure 1b) with a strong radioluminescence peak at 463 nm (Figure 1f). Theoretical modeling illustrates that at the initial conversion stage, the X-ray photons with the energy in the tens of keV interact with

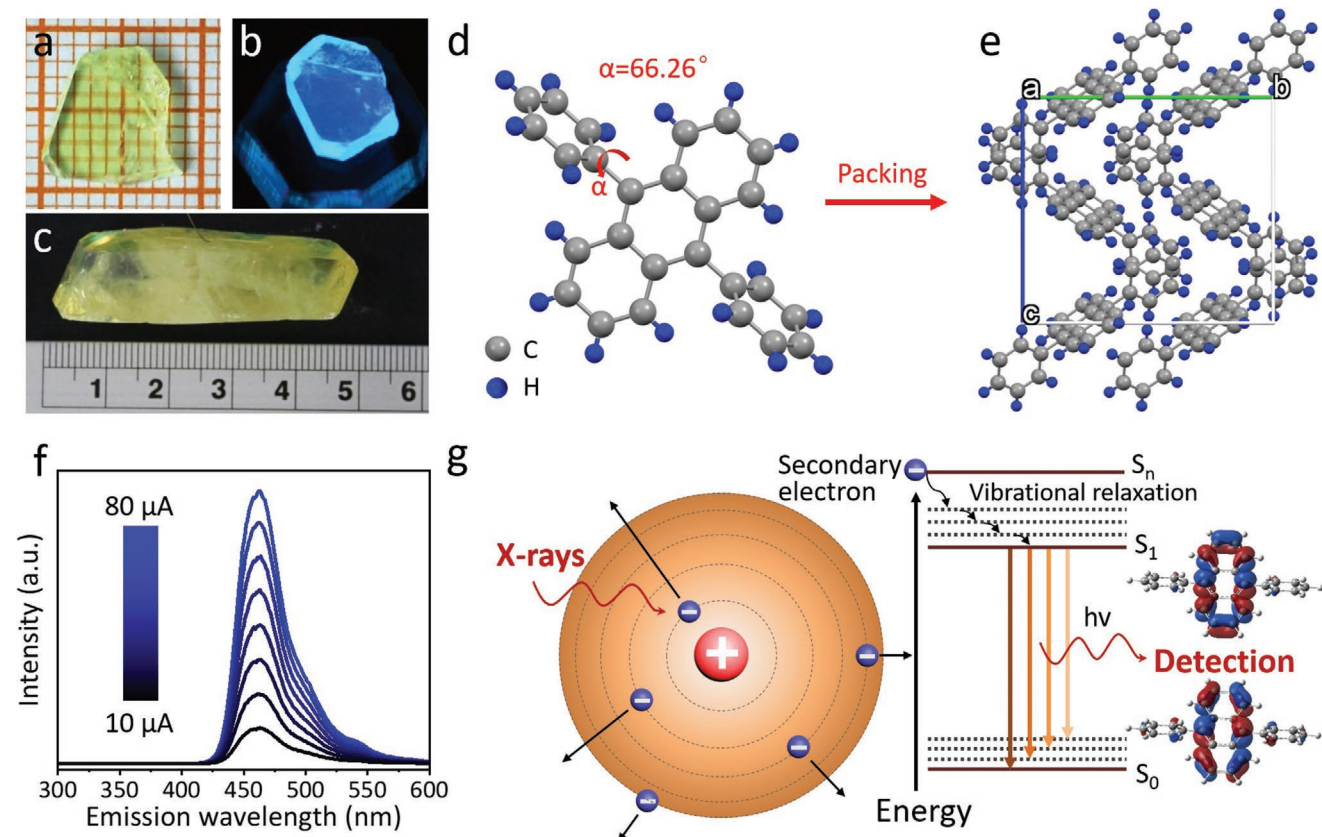


**Figure 1.** 9,10-DPA single crystals and their radioluminescence characteristics. a,b) Photographs of 9,10-DPA single crystals under ambient light and X-ray irradiation. c) Photographs of centimeter scale 9,10-DPA single crystal under ambient light. d) Molecular and e) crystal packing structure of 9,10-DPA. f) Normalized radioluminescence intensity of 9,10-DPA single crystals under X-ray excitation at a voltage of 50 kV with different currents. g) Schematic of theoretical modeling mechanism of 9,10-DPA single crystal under X-ray irradiation.

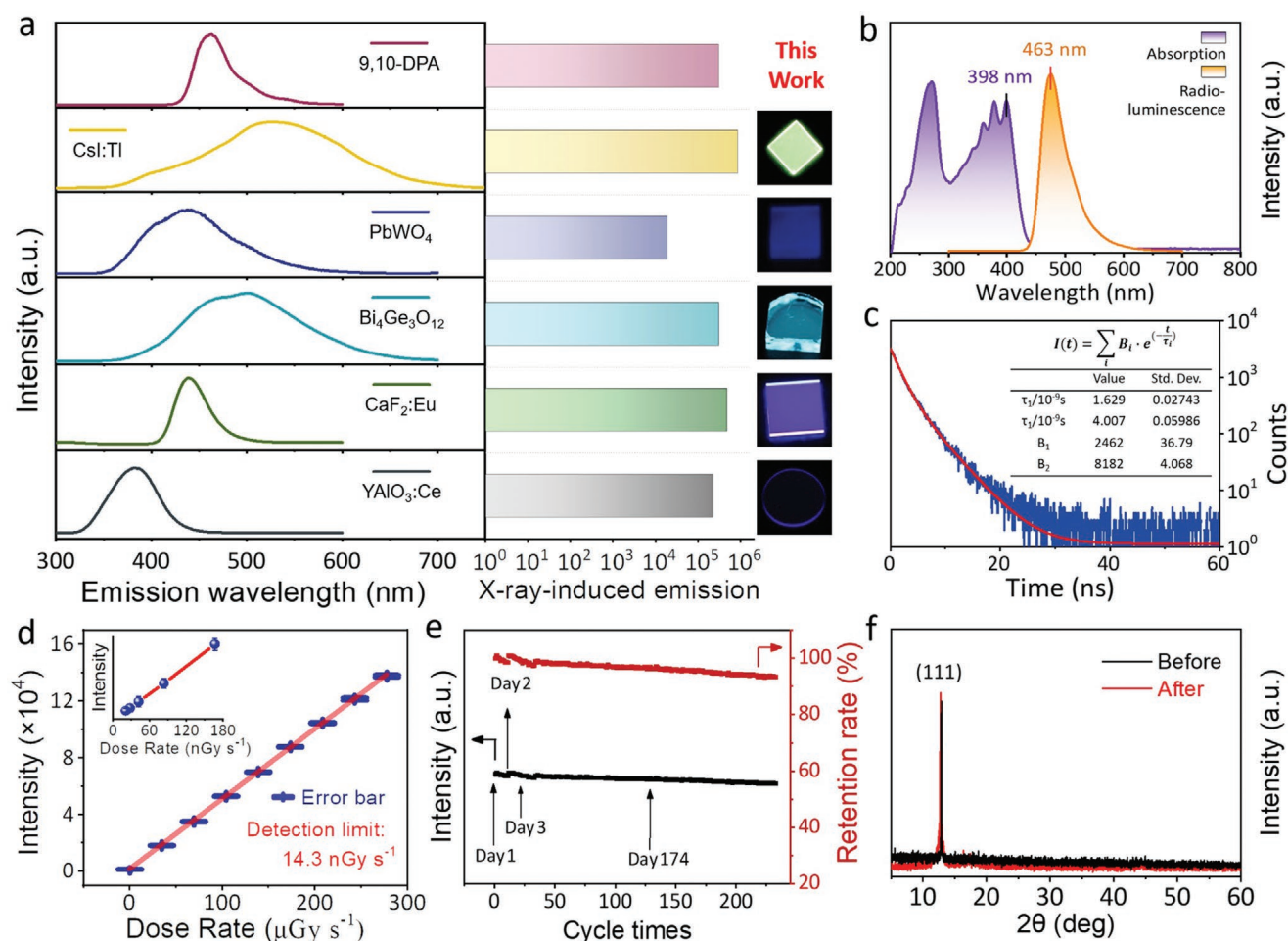


**Figure 2.** Sensitivity of 9,10-DPA single crystals for X-ray detection. a) Radioluminescence spectra and performance comparison of 9,10-DPA single crystals and conventional inorganic commercial scintillators under X-ray irradiation of 50 kV and 80  $\mu$ A, with the photographs of scintillators under X-ray illumination. b) Absorption and radioluminescence spectra of 9,10-DPA crystals. c) Decay time 1.63 ns for 9,10-DPA single crystals. d) Radioluminescence measurements for 9,10-DPA single crystals as a function of dose rate; the inset shows radioluminescence profiles measured at low dose rates. e) Stability after 233 cycle times over 174 days under X-ray illumination. f) XRD patterns of 9,10-DPA crystal before and after 233 cycle times of X-ray irradiation.

the electrons of the 9,10-DPA crystal, and a significant number of high-energy electrons and holes are generated (Figure 1g). Subsequently, the emitted high-energy electrons reach the lowest singlet S<sub>1</sub> after vibration relaxation and internal transfer, and thereafter transition back to the ground state S<sub>0</sub> in the form of radiation (see the “Experimental Section” and also Figure S2 in the Supporting Information).

The radioluminescence observed in our organic single crystals was compared with that of commercially available inorganic scintillators (CsI:Tl, PbWO<sub>4</sub>, Bi<sub>4</sub>Ge<sub>3</sub>O<sub>12</sub>, YAlO<sub>3</sub>:Ce, and CaF<sub>2</sub>:Eu) under the same conditions. The radioluminescence spectrum of the 9,10-DPA crystals displayed a maximum emission peak at 463 nm (Figure 2a) with a relatively narrow emission peak (full width at half maximum: FWHM  $\approx$  40 nm), which is significantly narrower than that of several other inorganic crystals. The radioluminescence intensity of the 9,10-DPA thin sheet crystal (Figure 1a) is comparable to that of commercially available inorganic scintillators (Table 1) under the same X-ray irradiation conditions (see Figure S3 in the Supporting

Information), indicating the significant potential of the 9,10-DPA crystals for X-ray detection.

The relative light yield of 9,10-DPA crystals has been reported to be 125% of anthracene,<sup>[32]</sup> and it could be calculated as 37% of CsI:Tl based on the integration of Figure 2a. It is generally known that low-Z elements exhibit low X-ray absorptivity (Figure S4, Supporting Information). However, the high radioluminescence intensity is the most important factor for indirect X-ray detection, which depends not only on the X-ray absorptivity, but also on the luminescence efficiency ( $\eta$ , ratio of the total energy of the emitted to absorbed photons). For instance, the PbWO<sub>4</sub> crystal yields the highest attenuation coefficient among the investigated samples under 18 keV (Figure S4, Supporting Information), but exhibits the lowest radioluminescence intensity (Figure 2a), which indicates its low luminescence efficiency and a significant amount of absorbed energy waste by nonradiative transition.

According to the absorbance and light yield, the relative luminescence efficiency ( $\eta_R$ ) versus CsI:Tl of 9,10-DPA crystals with



different thicknesses was calculated and plotted (Figure S5, Supporting Information; for the calculation process, see the “Experimental Section”). Although the absorbance of DPA crystals is lower, they exhibit considerably higher luminescence efficiency, which is  $\approx 5.3$  times higher than that of CsI:Tl with the same thickness ( $\approx 1$  mm). We note that with such a thick crystal, luminescence is more likely to escape from the edge of the crystal (as clearly observed in Figure 1b and in Figure S6, Supporting Information), and the visible-light detector above the crystal can only accept the photon signal emitted from the crystal surface. Thus, the photon-conversion efficiency was significantly underestimated. This light-trapping effect is reduced by decreasing the thickness of the 9,10-DPA crystals. Significantly, at 120  $\mu\text{m}$ , the photon-conversion efficiency of DPA crystals was  $\approx 33$  times that of CsI:Tl. Such a high photon-conversion efficiency is significantly beneficial for high-sensitivity X-ray detection.

The high photon-conversion efficiency of organic semiconductor single crystals fundamentally originates from their unique scintillation mechanism, which is different from that of inorganic crystals. In inorganic scintillators, electrons and holes are created by the interaction between lattice atoms and X-rays. The substantial amounts of hot excitons thereafter transfer energy to the luminescence centers, e.g.,  $\text{Tl}^+$ ,  $\text{Ce}^{3+}$ ,  $\text{Pr}^{3+}$ , or  $\text{Eu}^{2+}$  (Figure S7, Supporting Information),<sup>[11,33]</sup> and the scintillating process is completed by the recombination of electron–hole pairs. However, the migrating charge carriers may be self-trapped at nonluminescent centers, leading to nonradiative losses and possibly radiative recombination delays. In organic crystals, scintillation arises from the transitions between different molecular energy levels. When a molecule is excited via the absorption of X-ray energy from the ground to excited states, it returns to the ground state again and emits light, which mainly depends on the molecular structure instead of the luminous centers. In contrast, organic single crystals with long-range molecular packing order and a few grain boundaries exhibit great potential for X-ray detection.<sup>[34,35]</sup> In addition, the absorption and radioluminescence emission spectra of 9,10-DPA exhibited negligible overlap (Figure 2b), and the large Stokes shift resulted in negligible self-absorption and improved emission intensity.<sup>[36]</sup>

The luminescence decay time is an important parameter for evaluating the performance of a scintillator,<sup>[37,38]</sup> because the fast response allows more efficient photon emission, and significantly shortens the dead time for radio detection, thereby eliminating afterglow interference for instantaneous X-ray imaging. It is highly desirable that the organic crystals of 9,10-DPA exhibit fast response to X-ray illumination with a decay time of only 1.63 ns (Figure 2c; Table S2, Supporting Information), which is  $\approx 2$ –4 orders of magnitude shorter than those of conventional inorganic scintillators (e.g., CsI:Tl, decay time  $\approx 1000$  ns) (Table 1). The significantly faster photoluminescence (PL) decay time favors the competition between radiative and nonradiative recombinations and fundamentally contributes to their high photon-conversion efficiency.

The radioluminescence intensity of the organic crystal increased linearly with X-ray dose rates (Figure 2d; Figure S8, Supporting Information), exhibiting the lowest detectable dose rate of 14.3 nGy  $\text{s}^{-1}$  (using the  $3\sigma$  method),

which is  $\approx 380$  times lower than the dose of inorganic scintillators used for X-ray diagnostics (5.5  $\mu\text{Gy s}^{-1}$ ).<sup>[39]</sup> As we are aware, for industrial applications, it is suitable for high dose rate irradiation to obtain the best image quality; however, for medical applications, the dose rates must be maintained at the lowest level that is sufficient for the detection of lesion area to maximally reduce the damage to the human body.<sup>[40]</sup> Hence, the low-dose-rate detection limit of our organic crystals is of critical importance for medical imaging.

The stability and repeatability of the detection are also critical. We evaluated the stability of 9,10-DPA crystals using repeated cycle experiments. The radioluminescence peak remained identical at 463 nm (Figure S9, Supporting Information), and the intensity of radioluminescence maintains a retention rate of  $\approx 94\%$  after 233 cycles over 174 days under X-ray illumination (Figure 2e), demonstrating the high cycling stability of the organic crystals. Such cycling stability indicates no significant radiation damage, which may be partly attributed to the low absorption and high photon-conversion efficiency. Moreover, after keeping the organic crystals in air for 174 days, the X-ray diffraction (XRD) pattern (Figure 2f) and Raman spectra (Figure S10, Supporting Information) exhibit no clear change, which indicates its excellent environmental stability, with advantages over its deliquescent inorganic counterparts (Figure S11, Supporting Information).

The resolution of 9,10-DPA crystals for X-ray imaging was confirmed using a linear mask consisting of lines with widths ranging from 50 to 300  $\mu\text{m}$  (Figure S12, Supporting Information). Under X-ray synchrotron radiation with a photon energy of 18 keV, lines with an FWHM of 50  $\mu\text{m}$  can be clearly imaged (Figure 3a,b), demonstrating that the resolution of the organic single crystals will exceed 20.00 line pairs per millimeter (lp  $\text{mm}^{-1}$ ). Moreover, narrower linewidths for this evaluation are performed; for instance, the linewidth down to 40  $\mu\text{m}$  works well as well (Figure S13, Supporting Information). Plastic scintillators were used for comparison under the same conditions (Figure S14, Supporting Information); however, the obtained image is unclear, probably because of the weak radioluminescence intensity and poor homogeneity of the plastic scintillators. This may be an important reason why plastic scintillators are not commercially used for X-ray imaging. A vivid example of our organic crystal is used to image the logo of our university (Figure 3c,d), and the margin and inner details of the mask are clearly imaged, demonstrating the high resolution of the organic single crystals.

For practical applications, a setup for X-ray imaging is constructed as shown in Figure 3e. Test samples can be placed between the X-ray synchrotron radiation source and organic crystal. For instance, a metal needle was perfectly imaged (Figure S15, Supporting Information), even the plastic layers wrapping on the needle tip can be distinguished very well, confirming the applicability of our setup. Thereafter, a circuit board was placed in, and the obtained X-ray image is shown in Figure 3f. The X-ray transmittance through the circuit board is determined by the material of the circuit board and thicknesses of different metals; hence, the image presented by the 9,10-DPA crystal provides a very clear difference in brightness ranging from No.1 to No.4. Interestingly, when the magnesium–aluminum alloy was examined by our setup, even the

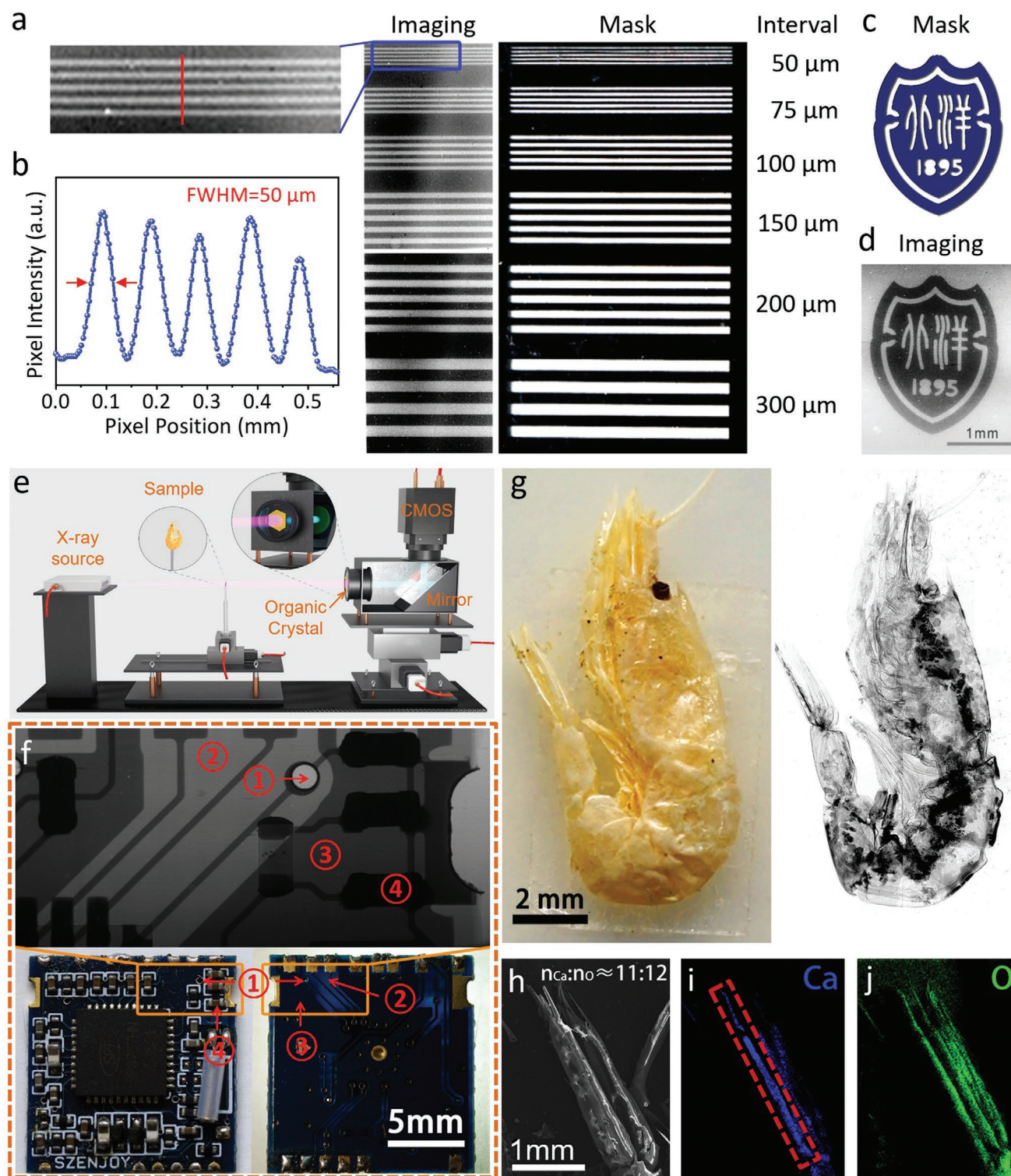


**Figure 3.** Practical application of the organic semiconductor single crystals for X-ray imaging. a) X-ray images of linear mask taken by 9,10-DPA crystals. b) Light-intensity function of pixels (along the red line above and FWHM is taken as the resolution) patterned millimeter-scale mask. c,d) X-ray images taken by 9,10-DPA single-crystal-based X-ray detector for the university logo. e) System schematic excited by an X-ray synchrotron radiation source. f) X-ray imaging for circuit board; the red numbers indicate the corresponding position photos and X-ray imaging. g) X-ray imaging for dried small shrimp. h) SEM image of dried small shrimp. i) Calcium mapping and j) oxygen mapping of the shrimp tail.



internal structure of the alloy could be inspected (Figure S16, Supporting Information). All results confirm that 9,10-DPA single crystals are expected to play an important role in nondestructive X-ray image detection and industrial flaw detection.<sup>[41]</sup>

These features are attractive for medical X-ray imaging because of their high sensitivity, high resolution, and low dose rate. Accordingly, a small dried shrimp (purchased as a food product from the WuMart Market) was used as a representative biological sample. Interestingly, not only the outline but also the inner details of the shrimp can be imaged clearly (Figure 3g). In order to confirm the imaging mechanism of the organic crystals, scanning electron microscopy (SEM) images and energy-dispersive X-ray spectroscopy (EDS) mapping were also performed (Figure 3h–j; Figure S17 and Table S3, Supporting Information). X-ray imaging reflects the mass-thickness contrast of an object under the test. The higher the atomic number  $Z$ , the thicker the sample, the greater the density, and the darker the imaging. For instance, calcium and oxygen are two abundant elements in shrimp tails. Apparently, the oxygen is homogeneously distributed, but calcium tends to be more on the left than on the right, which implies a higher density in the red square (Figure 3i). This is consistent with the lower X-ray transmittance owing to the high density and interaction with the metallic element, resulting in a darker image in the red square of the shrimp tail. The consistency of the results confirmed the applicability of our new organic crystals for biological X-ray imaging. Organic crystals are expected to have wide applications in the field of medical imaging, particularly under soft X-ray excitation in the future.

### 3. Conclusion

This study proposes low-temperature solution-grown organic semiconductor single crystals of 9,10-DPA for X-ray detection and imaging. They exhibit ultrafast radioluminescence with ultrahigh photon-conversion efficiency and make it highly promising for X-ray detection with ultralow detectable dose rate ( $14.3 \text{ nGy s}^{-1}$ ), and no significant afterglow interference for high-resolution (resolution  $> 20.00 \text{ lp mm}^{-1}$ ) instantaneous X-ray imaging. These findings demonstrate the potential for promising low-cost X-ray imaging technology, including medical diagnostics, X-ray security, and computed tomography in the future.

### 4. Experimental Section

**Materials and Chemicals:** The 9,10-DPA (CAS:1499-10-1, 98.0%+) was purchased from Ameko Co., Ltd. The *p*-xylene (CAS: 106-42-3, 99%+) and isopropyl alcohol (CAS: 67-63-0, 99%+) were purchased from TCI Co. The sodium hydride (CAS: 7646-69-7) was purchased from Tianjin Chemical Co. Commercial scintillators (CsI:Tl, PdWO<sub>3</sub>, Bi<sub>4</sub>Ge<sub>3</sub>O<sub>12</sub>, CaF<sub>2</sub>:Eu, and YAlO<sub>3</sub>:Ce) were purchased from Lation Technology Co. Plastic scintillators (No. EJ-212) were purchased from Eljen Technology Co.

**Purification:** In order to purify the 9,10-DPA, vacuum sublimation was used by a zone tube furnace. Raw material was placed in a quartz tube, and temperatures of sublimated and crystallized zones were set at 200 and 150 °C, respectively. High purity argon was used as the carrier gas (100 sccm). Pure 9,10-DPA was obtained at the low-temperature zone.

The *p*-xylene was redistilled with sodium hydride to remove residual water and impurities.

**Growth of 9,10-DPA Single Crystals:** The 9,10-DPA single crystals were grown by using the improved solution method. The 9,10-DPA powder was added into *p*-xylene until reaching saturation at 65 °C, forming a yellow solution. A small 9,10-DPA crystal was used as seed and placed into the saturated solution in a 1 L wide-mouthed bottle. The sealed bottle was put in thermostated water bath with the electric motor (Figure S1, Supporting Information). With the decrease of the solution temperature from 65 to 30 °C, the yellow crystal of 9,10-DPA was successfully grown after several days.

**Characterizations:** Optical images were recorded using a Sony camera (ILCE-6000, Japan). Raman measurements were performed with a high-resolution Raman microscope (RENISHAW, UK) in a backscattering configuration. The steady absorption spectra of crystals were performed on a UV-3600 Plus spectrometer (Shimadzu, Japan) using an integrating sphere. The steady PL was recorded in front-face mode with an Edinburgh instruments (FLS980) equipped with a Peltiercooled Hamamatsu R928-P PMT (200–900 nm) and corrected for the wavelength-dependent phototube response. Luminescence decays and photoluminescence quantum yield (PLQY) were measured with the same apparatus and a microsecond flash lamp (uF900) as an excitation source in multichannel scaling mode. A single crystal of 9,10-DPA with dimensions of  $\approx 0.1 \times 0.1 \times 0.1 \text{ mm}^3$  was selected and used for the single crystal diffraction experiment. Datasets were collected by using a Bruker SMART APEX-II diffractometer equipped with a CCD detector (Cu  $K\alpha$  radiation,  $\lambda = 0.154 \text{ nm}$ ) at 293 K. Data integration and cell refinement were performed by using the Olex2 software with the ShelXL method. XRD measurements were carried out in reflection mode at 45 kV and 200 mA with monochromatic Cu  $K\alpha$  radiation utilizing a Rigaku Smartlab diffractometer. The dried small shrimp was observed by high-angle annular dark-field scanning transmission electron microscopy (HAADF-SEM) (S-4800, Thermo), and EDS elemental mapping was carried out on at 20 kV.

**Luminescence Efficiency Discussion of 9,10-DPA Single Crystals:** To discuss the luminescence efficiency of 9,10-DPA single crystals, mass attenuation coefficients ( $\mu_m$ ) data were obtained from XCOM: Photon Cross Sections Database (Figure S4, Supporting Information).<sup>[42]</sup> Attenuation coefficients ( $\mu$ ) could be calculated by the following formula

$$\mu = \mu_m \times \rho \quad (1)$$

where  $\rho$  is the density of materials (see Table S1 in the Supporting Information). The intensity of X-ray transmission ( $I$ ) could be calculated by formula

$$I = I_0 \times e^{-\mu T} \quad (2)$$

where  $I_0$  is the incident intensity of X-ray and  $T$  is the thickness of materials. Therefore, the attenuation coefficients ( $\mu$ ) can be calculated by the slope of the formula (see Figure S18 in the Supporting Information)

$$\mu = -\frac{1}{T} \ln\left(\frac{I}{I_0}\right) \quad (3)$$

The absorbance ( $\epsilon$ ) of materials could be calculated by the formula

$$\epsilon = 1 - \frac{I}{I_0} = 1 - e^{-\mu T} \quad (4)$$

and luminescence efficiency ( $\eta$ ) could be calculated by the formula

$$\eta = \frac{E_{\text{vis}} N_{\text{ph}}}{E_{\text{abs}}} = \frac{E_{\text{vis}} N_{\text{ph}}}{\epsilon \times E} \quad (5)$$

where  $E$  is the energy of the incident X-rays,  $E_{\text{vis}}$  is the energy of the generated UV–vis photons, and  $N_{\text{ph}}$  is the counts of photons. The relative luminescence efficiency ( $\eta_r$ ) of 9,10-DPA with different thickness versus CsI:Tl ( $\approx 1 \text{ mm}$ ) was measured and plotted (Figure S5, Supporting Information).

**Decay Time Measurement of the 9,10-DPA Scintillator:** To compare the time resolution of 9,10-DPA scintillator and conventional bulk

scintillators, the time-resolved photoluminescence spectra of 9,10-DPA were measured. The multiexponential fit was widely applied to characterize the processes of radiative decay, which can be described by the formula

$$I(t) = A + \sum_i B_i \cdot e^{-\left(\frac{t}{\tau_i}\right)} \quad (6)$$

where  $I(t)$  represents the PL intensity at time  $t$ ,  $A$  the background,  $B_i$  the amplitude, and  $\tau_i$  the decay time constant.

**Density Functional Theory Calculation:** For the calculation of the projected partial density of states (PDOS), density functional theory (DFT) calculations were carried out. All DFT calculations were performed at B3LYP-D3/def2-TZVP<sup>[43,44]</sup> level by using the Gaussian 09 program. The radioluminescence spectra of 9,10-DPA crystal were computed by the time-dependent approach.<sup>[45]</sup> In order to illustrate the ground state  $S_0$  and the lowest singlet  $S_1$ , natural transition orbitals (NTOs) were generated with the help of Multiwfn program.<sup>[46]</sup>

**Radioluminescence Analysis using an X-ray Source:** The measurement of X-ray-induced luminescence was performed by using a reformed Edinburgh FS5 fluorescence spectrophotometer (Edinburgh Instruments Ltd., UK) equipped with a commercially miniature X-ray tube (AMPTEK, Inc.). The target in the X-ray tube was made of gold, and the maximum output was 4 W. The distance between the X-ray source 9,10-DPA and other commercially inorganic bulk scintillators was about 3 cm. The bandwidth of the emission spectra remained at 29 nm, and the dose of X-ray excitation could be changed by adjusting the voltage and current of the X-ray tube. The detection limit was derived from the slope of the fitting line and calculated on the  $3\sigma$ /slope method.

**X-ray Photoconductor Devices:** To fabricate the X-ray photoconductor device, quartz sheets were first cleaned by sonication in acetone and isopropyl alcohol separately. After drying with nitrogen flow, the silver conductive adhesives used as electrodes were coated on the substrate, and then the 9,10-DPA crystal thin sheet was fixed on the silver conductive adhesives. The miniaturized X-ray tube (AMPTEK, Inc.) was used as the X-ray source (cone angle of mini X-ray tube and normalized counts under different angles as shown in Figure S19 of the Supporting Information) with voltage and pulse current kept at 50 kV and 80  $\mu$ A, separately. The distance between the X-ray source and the device was about 2 cm. The current–voltage measurement was performed using a Keithley 4200 semiconductor parametric analyzer. All the experiments were carried out at ambient conditions.

**X-ray Detection and Imaging using an X-ray Synchrotron Radiation Source:** In an attempt to explore the resolution and imaging performance of the organic 9,10-DPA scintillators, synchrotron-radiation-based microcomputed tomography (SR $\mu$ CT) measurement was performed at the BL13W1 beamline of the Shanghai Synchrotron Radiation Facility (SSRF, Shanghai, China) using a monochromatic beam (the monochromatic source is a collimating light source, whose photon energy has a certain and adjustable value from 8 to 72.5 keV) with an energy of 18 keV and a sample-to-detector distance of 0.5 m. In the study, a complementary metal–oxide–semiconductor detector (2048  $\times$  2048 pixels, Flash 4.0, Hamamatsu City, Japan) with the pixel size set to 3.25  $\mu$ m was used to record images.

## Supporting Information

Supporting Information is available from the Wiley Online Library or from the author.

## Acknowledgements

The authors sincerely acknowledge Dr. Ke Li and Dr. Yanan Fu (BL13W1, Shanghai Synchrotron Radiation Facility) for help with X-ray imaging, Dr. Zheyuan Liu for help to conduct DFT calculations and

structure simulations, and Dr. Cong Wang for help with proof-reading and suggestions. This work was supported financially by the Ministry of Science and Technology of China (Grant No. 2017YFA0204503), National Natural Science Foundation of China (Grant Nos. 51733004, 51633006, and 51703160), and National Natural Science Foundation of China (Grant Nos. 91433115, 21473222, and 21661132006) and Chinese Academy of Sciences.

## Conflict of Interest

The authors declare no conflict of interest.

## Author Contributions

W.H. and X.D. designed and guided the project. M.C. prepared the 9,10-DPA crystals and performed X-ray excitation-related characterizations. X.O., X.L., and H.Y. assisted the tests of X-ray detection. L.S. and H.D. carried out the PLQY, decay time measurements, and Raman spectra. M.C., W.H., and X.D. co-wrote the manuscript. All authors discussed the results and reviewed the manuscript.

## Data Availability Statement

Research data are not shared.

## Keywords

indirect X-ray detection, organic semiconductor single crystals, X-ray imaging

Received: June 21, 2021

Revised: August 10, 2021

Published online:

- [1] G. Blasse, B. C. Grabmaier, *Luminiscant Materials*, Springer-Verlag, Berlin/Heidelberg, Germany **1994**.
- [2] V. V. Nagarkar, T. K. Gupta, S. R. Miller, Y. Klugerman, M. R. Squillante, G. Entine, *IEEE Trans. Nucl. Sci.* **1998**, *45*, 492.
- [3] H. Wei, D. DeSantis, W. Wei, Y. Deng, D. Guo, T. J. Savenije, L. Cao, J. Huang, *Nat. Mater.* **2017**, *16*, 826.
- [4] Z. Du, X. Zhang, Z. Guo, J. Xie, X. Dong, S. Zhu, J. Du, Z. Gu, Y. Zhao, *Adv. Mater.* **2018**, *30*, 1804046.
- [5] W. C. Röntgen, *Science* **1896**, *3*, 227.
- [6] M. Hoheisel, *Nucl. Instrum. Methods Phys. Res., Sect. A* **2006**, *563*, 215.
- [7] B. Fraboni, A. Fraleoni-Morgera, N. Zaitseva, *Adv. Funct. Mater.* **2016**, *26*, 2276.
- [8] W. Pan, H. Wu, J. Luo, Z. Deng, C. Ge, C. Chen, X. Jiang, W.-J. Yin, G. Niu, L. Zhu, L. Yin, Y. Zhou, Q. Xie, X. Ke, M. Sui, J. Tang, *Nat. Photonics* **2017**, *11*, 726.
- [9] P. Büchele, M. Richter, S. F. Tedde, G. J. Matt, G. N. Ankah, *Nat. Photonics* **2015**, *9*, 843.
- [10] R. E. Hofstadter, *Phys. Rev.* **1949**, *75*, 796.
- [11] T. J. Hajagos, C. Liu, N. J. Cherepy, Q. Pei, *Adv. Mater.* **2018**, *30*, 1706956.
- [12] N. Yasui, Y. Ohashi, T. Kobayashi, T. Den, *Adv. Mater.* **2012**, *24*, 5464.
- [13] M. Nikl, A. Yoshikawa, *Adv. Opt. Mater.* **2015**, *3*, 463.
- [14] C. W. E. van Eijk, *Nucl. Instrum. Methods Phys. Res., Sect. A* **2001**, *460*, 1.

- [15] M. J. Weber, *J. Lumin.* **2002**, *100*, 35.
- [16] E. V. D. van Loef, P. Dorenbos, C. W. E. van Eijk, *Appl. Phys. Lett.* **2001**, *79*, 1573.
- [17] B. K. Cha, J. H. Bae, C. Lee, H. Jeon, H. Kim, S. Chang, B.-S. Kang, G. Cho, *Nucl. Instrum. Methods Phys. Res., Sect. A* **2009**, *607*, 145.
- [18] F. Maddalena, L. Tjahjana, A. Xie, A. Arramel, S. Zeng, H. Wang, P. Coquet, W. Drozdowski, C. Dujardin, C. Dang, D. Birowosuto, *Crystals* **2019**, *9*, 88.
- [19] Y. Zhang, R. Sun, X. Ou, K. Fu, Q. Chen, Y. Ding, L.-J. Xu, L. Liu, Y. Han, A. Malko, X. Liu, H. Yang, O. M. Bakr, H. Liu, O. F. Mohammed, *ACS Nano* **2019**, *2*, 2520.
- [20] Y. Wang, X. Yin, W. Liu, J. Xie, J. Chen, M. A. Silver, D. Sheng, L. Chen, J. Diwu, N. Liu, Z. Chai, T. E. Albrecht-Schmitt, S. Wang, *Angew. Chem., Int. Ed.* **2018**, *57*, 7883.
- [21] S. Chen, *Science* **2018**, *359*, 1452.
- [22] C. Wang, H. Dong, W. Hu, Y. Liu, D. Zhu, *Chem. Rev.* **2012**, *112*, 2208.
- [23] C. W. E. van Eijk, P. Dorenbos, E. V. D. van Loef, K. Krämer, H. Güdel, *Radiat. Meas.* **2001**, *33*, 521.
- [24] S. E. Derenzo, W. W. Moses, J. L. Cahoon, R. C. C. Perera, J. E. Litton, *IEEE Trans. Nucl. Sci.* **1990**, *37*, 203.
- [25] Z. S. Macedo, R. S. Silva, M. E. G. Valerio, A. L. Martinez, A. C. Hernandez, *J. Am. Ceram. Soc.* **2004**, *87*, 1076.
- [26] I. Holl, E. Lorenz, G. Mageras, *IEEE Trans. Nucl. Sci.* **1988**, *35*, 105.
- [27] M. Moszynski, T. Ludziejewski, D. Wolski, W. Klamra, L. O. Norlin, *Nucl. Instrum. Methods Phys. Res., Sect. A* **1994**, *345*, 461.
- [28] Q. Li, Z. Li, *Adv. Sci.* **2017**, *4*, 1600484.
- [29] J. Chen, C. C. W. Law, W. Jacky, Y. Dong, S. M. F. Lo, I. D. Williams, D. B. Zhu, B. Z. Tang, *Chem. Mater.* **2003**, *15*, 1535.
- [30] X. Li, Y. Wu, S. Zhang, B. Cai, Y. Gu, J. Song, H. Zeng, *Adv. Funct. Mater.* **2016**, *26*, 2435.
- [31] Y. Wang, J. Yang, Y. Gong, M. Fang, Z. Li, B. Z. Tang, *SmartMat* **2020**, *1*, e1006.
- [32] E. V. van Loef, J. Glodo, U. Shirwadkar, N. Zaitseva, K. S. Shah, *Nucl. Instrum. Methods Phys. Res., Sect. A* **2011**, *652*, 424.
- [33] B. Fraboni, A. Ciavatti, F. Merlo, L. Pasquini, A. Cavallini, A. Quaranta, A. Bonfiglio, A. Fraleoni-Morgera, *Adv. Mater.* **2012**, *24*, 2289.
- [34] A. Ciavatti, E. Capria, A. Fraleoni-Morgera, G. Tromba, D. Dreossi, P. J. Sellin, P. Cosseddu, A. Bonfiglio, B. Fraboni, *Adv. Mater.* **2016**, *27*, 7213.
- [35] D. Zhao, M. Xu, B. Xiao, B. Zhang, L. Yan, G. Zeng, A. Dubois, P. Sellin, W. Jie, Y. Xu, *J. Mater. Chem. A* **2020**, *8*, 5217.
- [36] X. Q. Ou, B. Huang, J. Zan, Q. Wu, Z. Hong, L. Xie, H. Bian, Z. Yi, X. Chen, Y. Wu, X. Song, J. Li, Q. Chen, H. Yang, X. Liu, *Nature* **2021**, *590*, 410.
- [37] J. A. Steele, W. Pan, C. Martin, M. Keshavarz, E. Debroye, H. Yuan, S. Banerjee, E. Fron, D. Jonckheere, C. W. Kim, W. Baekelant, G. Niu, J. Tang, J. Vanacken, M. van der Auweraer, J. Hofkens, M. B. J. Roeffaers, *Adv. Mater.* **2018**, *30*, 1804450.
- [38] Q. Chen, J. Wu, X. Ou, B. Huang, J. Almutlaq, A. A. Zhumekenov, X. Guan, S. Han, L. Liang, Z. Yi, J. Li, X. Xie, Y. Wang, Y. Li, D. Fan, D. B. L. Teh, A. H. All, O. F. Mohammed, O. M. Bakr, T. Wu, M. Bettinelli, H. Yang, W. Huang, X. Liu, *Nature* **2018**, *561*, 88.
- [39] H. B. Phillips, R. K. Swank, *Rev. Sci. Instrum.* **1953**, *24*, 611.
- [40] M. K. Kalra, M. M. Maher, T. L. Toth, L. M. Hamberg, M. A. Blake, J.-A. Shepard, S. Saini, *Radiology* **2004**, *230*, 619.
- [41] J. H. Heo, D. H. Shin, J. K. Park, D. H. Kim, S. J. Lee, S. H. Im, *Adv. Mater.* **2018**, *30*, 1801743.
- [42] M. J. Berger, XCOM: Photon Cross Sections Database, <https://www.nist.gov/pml/xcom-photon-cross-sections-database> (accessed: February 2021).
- [43] S. Grimme, S. Ehrlich, L. Goerigk, *J. Comput. Chem.* **2011**, *32*, 1456.
- [44] F. Weigend, R. Ahlrichs, *Phys. Chem. Chem. Phys.* **2005**, *7*, 3297.
- [45] Y. J. Yan, S. Mukamel, *J. Chem. Phys.* **1986**, *85*, 5908.
- [46] T. Lu, F. Chen, *J. Comput. Chem.* **2012**, *33*, 580.